

# Triple Crossed Flexure Pivot Based on a Zero Parasitic Center Shift Kinematic Design

E. Thalmann<sup>1</sup>

Micromechanical and Horological Design Laboratory (Instant-Lab),  
École Polytechnique Fédérale de Lausanne (EPFL),  
Rue de la Maladière 71b,  
CH-2000 Neuchâtel, Switzerland  
e-mail: etienne.thalmann@epfl.ch

S. Henein

Micromechanical and Horological Design Laboratory (Instant-Lab),  
École Polytechnique Fédérale de Lausanne (EPFL),  
Rue de la Maladière 71b,  
CH-2000 Neuchâtel, Switzerland  
e-mail: simon.henein@epfl.ch

*Thanks to their absence of play, absence of contact friction and possible monolithic fabrication, flexure pivots offer advantages over traditional bearings in small-scale, high accuracy applications and environments where lubrication and wear debris are proscribed. However, they typically present a parasitic center shift that deteriorates their rotational guidance accuracy. Existing solutions addressing this issue have the drawbacks of reducing angular stroke, prohibiting planar design, or introducing overconstraints or underconstraints. This article presents a new triple crossed flexure pivot we have named TRIVOT whose kinematics theoretically nullify its parasitic center shift without overconstraints nor internal mobility. In the physical implementation, the center shift is non-zero but we show using the finite element method (FEM) that it is reduced by one order of magnitude in comparison to the widely used crossed flexure pivot (CFP). This allows to choose a crossing ratio of the flexures that either maximizes the angular stroke limit for given flexures or results in a compact planar design with the possibility of a remote center of compliance (RCC). Based on a pseudo-rigid-body model (PRBM), formulas for the rotational stiffness and angular stroke limit of the TRIVOT are derived, which are then validated by FEM. Finally, we show that a high support stiffness can be achieved based on a preliminary study for a mechanical watch time base application. We expect this new pivot to become a competitive alternative to the standard CFP for applications where high accuracy and compactness are required.*

[DOI: 10.1115/1.4053471]

**Keywords:** compliant mechanisms, mechanism design, flexure pivot, flexure hinge, parasitic center shift, remote center compliance

## 1 Introduction and Statement of Results

Flexure pivots, which use the elastic deformation of slender beams to guide a rotational motion, are attractive alternatives to traditional bearings for a wide range of applications where high accuracy and absence of contact friction are desired. Such applications include micromanipulation devices [1–5], aerospace mechanisms [6–8], medical devices [9–11], and watchmaking [12–14]. Flexure pivots,

however, face limitations in comparison to bearings such as a parasitic shift of their rotation axis, limited stroke, complex designs, overconstraints, or internal degrees-of-freedom. For instance, the crossed flexure pivot (CFP) (as known as cross-spring pivot) introduced by Wittrick [8,15–21] can either have a minimal parasitic shift, a planar design, or the maximal admissible stroke for given leaf springs. Other pivots achieve a large stroke, a very small parasitic shift, and a planar design using serial arrangements of flexures, such as the “Butterfly” pivot [7] or the multi-stage compound radial flexure [22]. These architectures, however, have the drawback of having internal (redundant) degrees-of-freedom that can be excited by vibrations or need external slaving mechanisms to be suppressed [23,24]. Alternatively, the gravity-insensitive flexure pivot (GIFP) developed in previous joint work [13,25] allows to optimally distribute the stress in the flexures and significantly reduce the parasitic shift in comparison to the CFP, but at the expense of compactness. The co-RCC pivot also developed in previous joint work [26–28] presents an alternative way of reducing the parasitic center shift while having a planar design but the remaining center shift is not negligible [13]. Other solutions exist to tackle the issue of parasitic shift while maximizing angular stroke or having a planar design, but they are either overconstrained [29] or have additional elasticity at one extremity [30].

In this paper, we present a new TRIPle crossed flexure piVOT (TRIVOT) with the following advantages:

- The kinematics of the TRIVOT theoretically nullify its parasitic center shift. In practice, the ideal kinematic joints are approximated by flexures that present residual kinematic defects. Nevertheless, the center shift is reduced by one order of magnitude in comparison to the standard CFP.
- Unlike the CFP, the parasitic shift is reduced for any crossing ratio of the TRIVOT flexures. This allows to choose either the ratio that maximizes the angular stroke for given flexures or a ratio that enables a planar design that is beneficial for manufacturing and compactness.
- The center of rotation of the TRIVOT can be placed outside of the physical structure of the flexures (pure rotation about a virtual point). This property called *remote center compliance* (RCC) [24,31,32] could previously only be achieved with a parasitic shift [18,32] or with serial compensations that add complexity or internal degrees-of-freedom [1,22,33].

This paper is an extended version of work presented at the Mechanisms and Robotics Conference at ASME IDETC 2021 [34]. We first give a detailed description of the TRIVOT design and its variants (Sec. 2). We then develop a pseudo-rigid-body model (PRBM) of the TRIVOT (Sec. 3). Based on this model, we analyze its parasitic shift (Sec. 4.2) and derive formulas for the rotational stiffness (Sec. 4.3) and admissible angular stroke (Sec. 4.4). These results are validated using the finite element method (FEM) and compared to a benchmark, the CFP. Finally, we analyze the support stiffness of the TRIVOT based on an application as mechanical watch oscillator and provide ways to improve it (Sec. 5).

## 2 Design of the TRIVOT Flexure Pivot

**2.1 General Kinematics.** As a first step to the flexure implementation of Sec. 2.3, we give a step-by-step description of the TRIVOT design based on the two-dimensional kinematic diagram with ideal pivots in Fig. 1:

- (a) Figure 1(a) illustrates the fundamental definition of virtual pivot. It consists of a *mobile body* rotating with respect to a *fixed body* about a virtual center  $O$ , which we call the center of the mechanism.
- (b) In order to realize Fig. 1(a), bearings are required. These consist of three parallel kinematic chains connecting the mobile body to the fixed one (Fig. 1(b)). Each chain consists of a *main connecting rod*, with a pivot joint at each extremity, in series with a *radial slider* joint. The connecting rods all

<sup>1</sup>Corresponding author.

Contributed by the Mechanisms and Robotics Committee of ASME for publication in the JOURNAL OF MECHANISMS AND ROBOTICS. Manuscript received October 15, 2021; final manuscript received December 21, 2021; published online February 18, 2022. Assoc. Editor: Guangbo Hao.

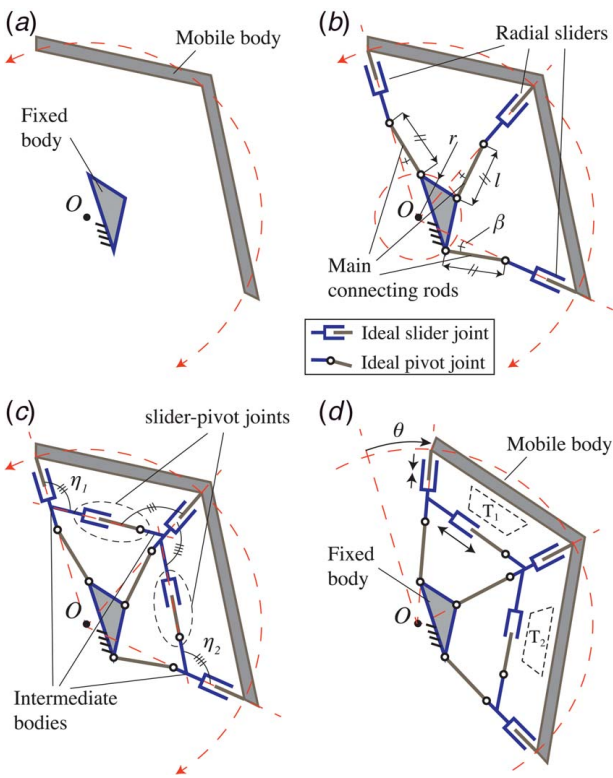


**Fig. 1 Step-by-step description of the TRIVOT kinematics:** (a) fixed and mobile bodies, (b) addition of the kinematic chains connecting the mobile body to the fixed one, (c) coupling of the intermediate bodies with slider-pivot joints, and (d) rotation of the system to the neutral position. See video<sup>2</sup>.

have the same length  $l$  and are attached to the fixed body at the same distance  $r$  from point  $O$ . The axes of the radial sliders are concurrent at point  $O$ . This enables the distance between the mobile body and point  $O$  to stay constant while the structure rotates, which is key to canceling the parasitic center shift. The connecting rods each form the same angle  $\beta$  with the axis of the radial slider to which they are attached. It follows that there exists a *neutral* position of the mobile body (Fig. 1(d)) in which the axes of the connecting rods are concurrent at point  $O$ , i.e.,  $\beta=0$ .

(c) The *intermediate bodies* between the connecting rods and the mobile body are connected in pairs by two *slider-pivot* kinematic chains (Fig. 1(c)). The sliding axis of each chain forms the same angles  $\eta_1$ , respectively,  $\eta_2$ , with the two adjacent radial slider axes. The result of this coupling can be seen in the shape of two isosceles trapezoids formed by the mobile body and the sliding axes ( $T_1$  and  $T_2$  in Fig. 1(d)). This ensures that the radial sliders always perform the same motion. It follows that the motion of the intermediate bodies is concentric with respect to  $O$ .

As a result of this geometry, the mobile body only has one degree-of-freedom (DOF): a pure rotation about point  $O$  described by the angle  $\theta$ , see Fig. 1(d) and video.<sup>2</sup> In comparison to an architecture without intermediate bodies like the CFP, the radial sliders absorb the parasitic motion of the connecting rod's mobile end, hence canceling it. Since there are no internal degrees-of-freedom, Grubler's formula for planar linkages [35] shows that the mobility  $M=1$  is obtained without overconstraint:

$$M = \sum_{i=1}^j f_i - 3(j - N + 1) = 13 - 3(13 - 10 + 1) = 1 \quad (1)$$

In this formula,  $N=10$  is the number of bodies and  $j=13$  is the number of joints with each a DOF  $f_i=1$ . Note that the fixed and mobile parts of the pivot are interchangeable.

**2.2 Symmetrical Design.** In order to have a 60 deg rotational symmetry of the architecture, which has the advantages of improving the mass distribution relative to  $O$  and reducing the differences in radial support stiffness in the flexure implementation, the general design depicted in Fig. 1(c) was modified as follows (Fig. 2):

- The connecting rods were fixed at the vertices of an equilateral triangle.
- An additional kinematic chain was added between the intermediate bodies.
- The neutral position was chosen as nominal.

Note that an *extra DOF* was added to avoid overconstraining the mechanism with the added kinematic chain (Fig. 2(a)). This is verified by Grubler's formula, which shows that the mobility  $M=1$  was obtained without overconstraint, see Eq. (1)

$$M = 16 - 3(16 - 12 + 1) = 1 \quad (2)$$

**2.3 Flexure Implementation.** The physical flexure implementation of the TRIVOT, for instance in Fig. 2(b), can be obtained from the kinematic diagrams in Figs. 1 and 2 as follows:

- The connecting rods are embodied by leaf springs which have equivalent kinematic behavior [24,36]. Since the deformation of these flexures is proportional to the rotation of the TRIVOT (Sec. 3.1), we call them *main* flexures.
- The radial sliders are embodied by parallel leaf springs whose parabolic motion is known to closely approximate translations for small displacements [24]. Since the deformation of these flexures is of second order of the rotation of the TRIVOT (see Sec. 3.2), we categorize them as *secondary* flexures.
- The slider-pivot kinematic chains are embodied by leaf springs perpendicular to the sliding axis whose motion closely approximates a pin-in-slot joint for small displacements [24]. Since the deformation of these flexures is of second order of the rotation of the TRIVOT (see Sec. 3.3), we also categorize them as *secondary* flexures.
- The extra DOF can be implemented by locally reducing the thickness of one of the intermediate bodies, which essentially corresponds to a notch flexure hinge [24]. For symmetry reasons, we decided to omit this DOF in the flexure implementations of this article, assuming that our designs can be monolithically fabricated, i.e., do not need assembly and that there is enough flexibility in the system to release the overconstraint.

A mock-up was fabricated to validate the design qualitatively (Fig. 3). This setup demonstrated that the design behaves qualitatively as a pivot: the system has one DOF and the motion of the mobile body closely approximates a rotation about point  $O$ , see video.<sup>2</sup>

**2.4 Crossing Ratio  $\lambda$  of the Flexures.** Two different types of physical TRIVOT architectures can be categorized according to the point at which the main flexures cross. This point is defined using the dimensionless ratio  $\lambda=R/L$  where  $R$  is the distance from the center of the system  $O$  to the mobile extremities of the main flexures (in neutral position) and  $L$  is the length of these flexures (Fig. 2(b)). It follows that

- When  $\lambda \geq 1$ ,  $R \geq L$  and the main flexures cross virtually at point  $O$ , outside of their physical structure (Fig. 2(b)). This has the benefits of a planar design ( $\lambda=1.1$  in Fig. 3), which is advantageous for compactness and manufacturing, and potentially a RCC configuration (Fig. 1).

<sup>2</sup><https://youtu.be/rUH3cDmeXC4>

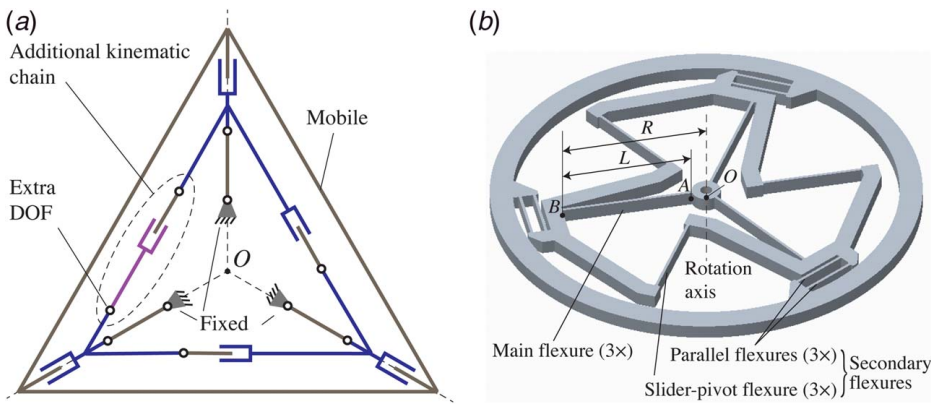


**Fig. 2 Symmetrical TRIVOT: (a) kinematic diagram and (b) flexure implementation**

- (b) When  $\lambda < 1$ ,  $L > R$  and the main flexures cross physically at the center of the mechanism (Fig. 4(a)). This has the benefit of better distributing the stress within the flexures (Sec. 4.4) but requires a physical implementation allowing the flexures to cross. An example of such architecture using three planes is depicted in Fig. 4.

Beyond characterizing the type of physical architecture, the crossing ration  $\lambda$  determines the main mechanical properties of the TRIVOT. This is due to the fact that the main flexures are subjected to the main deformation during the motion of the TRIVOT (see Remark 1). This parameter and its influence are analogous to the crossing ratio of the flexures of the well-known CFP, which has been widely studied in the literature [15,16,19,20]. Indeed, the fixed-guided boundary conditions of the flexures are the same in both architectures.

### 3 Pseudo-Rigid-Body Model

In order to derive analytical formulas for the kinematic and elastic properties of the TRIVOT, we use the pseudo-rigid-body model (PRBM) approach initially presented by Howell [37]. This provides a simple way of analyzing the motion and force of flexure mechanisms using a rigid-body mechanism with equivalent behavior. Following this principle, a PRBM approximating the behavior of the

TRIVOT can be derived from the kinematic diagrams in Figs. 1 and 2 as follows (Fig. 5):

- Torsional springs with spring constant  $k_t$  are added to the fixed extremity of the connecting rods. This corresponds to the PRBM developed by Pei et al. [38] for a flexure with one fixed extremity  $A$  and a mobile extremity  $B$  guided such that the tangent of the deflected curve at this point intersects point  $O$ , as is the case for the main flexures. In this model, the guided pivot is placed at the extremity  $B$  of the flexure and the fixed pivot  $C$  with torsional spring is placed at a distance  $\gamma L$  from point  $B$ .
- Linear springs with spring constant  $k_s$  are added to the radial sliders. The spring constant corresponds to the translational stiffness of the parallel flexure stage given in Ref. [39, Eq. (5.9)].
- Linear springs with spring constant  $k_{sp}$  are added to the sliders of the slider-pivot joints. The spring constant corresponds to the force-displacement characteristic of a flexure whose extremity goes through a lateral deflection such that the angular deflection at the end remains constant [39, Eq. (5.8)]. Note that this stiffness is equal to half the translational stiffness of a parallel stage with the same flexures. No torsional springs are added to the pivots of these slider-pivot joints since they have no motion during the rotation of the model, see Fig. 5(b).

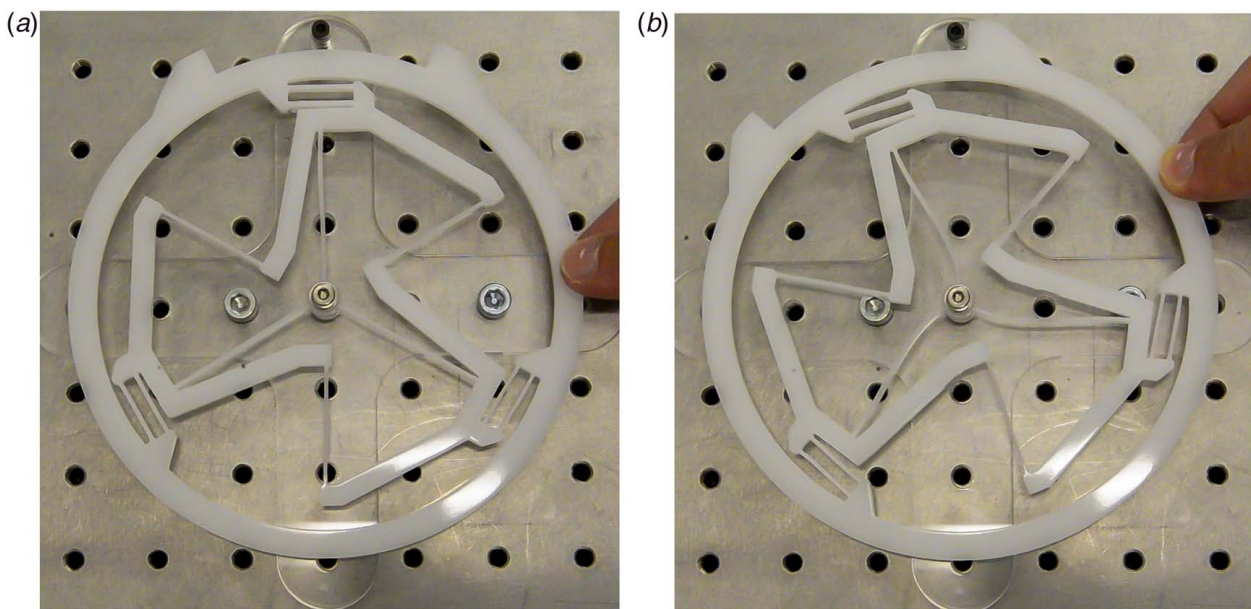


**Fig. 3 Mock-up of the planar TRIVOT with an outer diameter of 150 mm fabricated by laser cutting a  $b = 5$  mm thick POM sheet:** (a) nominal position and (b) rotated by 22 deg. See video.<sup>2</sup>

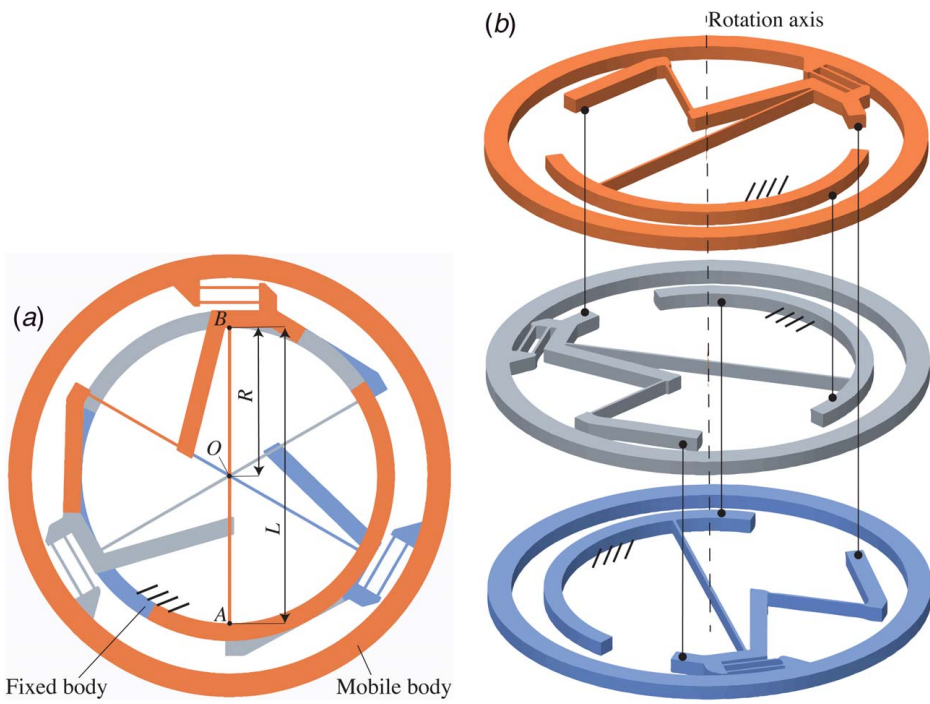


**Fig. 4 Flexure implementation of the TRIVOT with crossed flexures ( $\lambda < 1$ ): (a) top view and (b) exploded view. The lines with points at their extremities show the connections between rigid bodies across the three planes.**

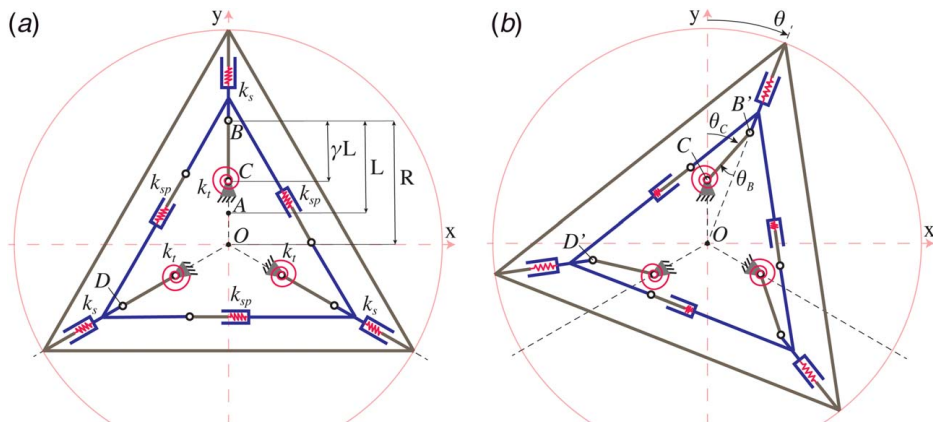


**Fig. 5 PRBM of the symmetrical TRIVOT in (a) neutral position and (b) rotated by an angle  $\theta$**

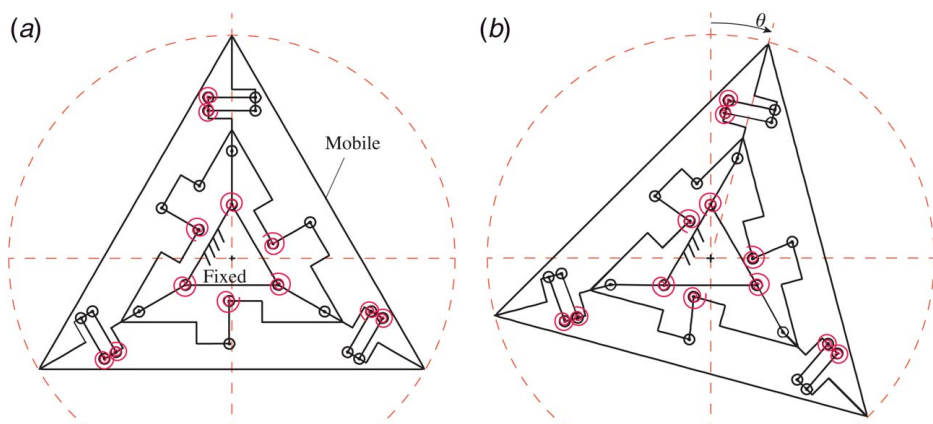


**Fig. 6 Advanced PRBM of the symmetrical TRIVOT in (a) nominal position and (b) rotated by angle  $\theta$ . See video.<sup>2</sup>**

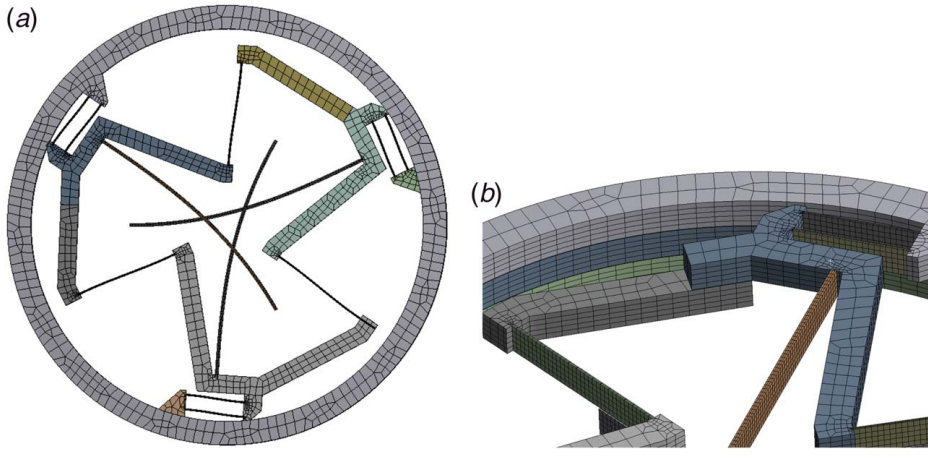


**Fig. 7 Finite element model of the TRIVOT: (a) 25 deg rotation with  $\lambda = 0.6$  and (b) close-up view of the mesh**

The next step is to compute the motion of the joints of the PRBM for a given rotation  $\theta$  of the symmetrical TRIVOT. This will give insights on the contributions of the different types of flexures and will be useful to calculate the elastic properties of this system. To simplify the model, knowing that flexure mechanisms have a limited range of motion, it is assumed that  $\theta$  is small and we express terms using series expansions around  $\theta=0$ .

**3.1 Motion of the Pivots of the Connecting Rods.** The angles  $\theta_C$  and  $\theta_B$  swept by the pivots of the connecting rods when the system rotates by an angle  $\theta$  are obtained by trigonometry, see Fig. 5(b):

$$\theta_B = \arcsin\left(\frac{|OC| \sin \theta}{|CB|}\right) \quad \theta_C = \theta + \theta_B \quad (3)$$

Knowing that  $|OC| = R - \gamma L$ ,  $|CB| = \gamma L$  and that [38, Eq. (11)]

$$\gamma = \frac{15\lambda^2}{18\lambda^2 - 3\lambda + 2} \quad (4)$$

using series expansions around  $\theta=0$  yields:

$$\begin{aligned} \theta_B &= \frac{2}{15} \theta \left( 9\lambda + \frac{1}{\lambda} - 9 \right) + \frac{\theta^3 (9\lambda^2 - 9\lambda + 1)(18\lambda^2 - 33\lambda + 2)(18\lambda^2 - 3\lambda + 2)}{10125\lambda^3} + \mathcal{O}(\theta^5) \\ \theta_C &= \theta \left( \frac{2}{15} \left( 9\lambda + \frac{1}{\lambda} - 9 \right) + 1 \right) + \frac{\theta^3 (9\lambda^2 - 9\lambda + 1)(18\lambda^2 - 33\lambda + 2)(18\lambda^2 - 3\lambda + 2)}{10125\lambda^3} + \mathcal{O}(\theta^5) \end{aligned} \quad (5)$$

**3.2 Motion of the Radial Sliders.** The motion of these sliders corresponds to the change in distance  $\Delta_s$  between the mobile and intermediate bodies along their respective sliding axis. This also corresponds to the opposite of the change in distance  $|OB'|$  between the center of rotation and the mobile extremity of the connecting rods:

$$\Delta_s(\theta) = |OB'(0)| - |OB'(\theta)| = |OB| - (|OC| \cos \theta + |CB| \cos \theta_B) \quad (6)$$

which, substituting Eq. (5) and using series expansion, yields

$$\Delta_s(\theta) = \frac{9\lambda^2 - 9\lambda + 1}{15\lambda} R\theta^2 + \mathcal{O}(\theta^4) \quad (7)$$

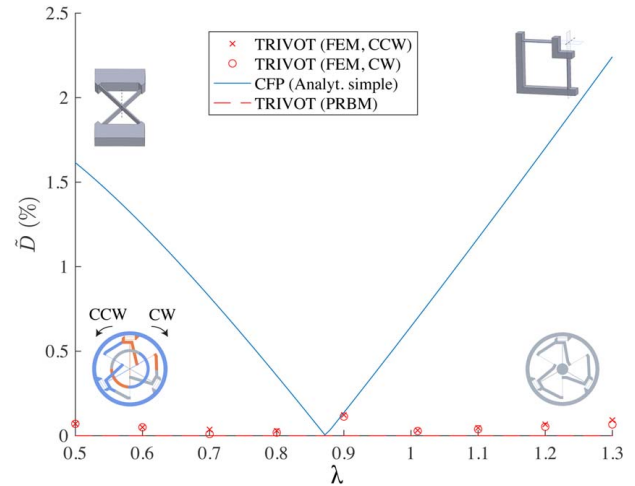


**Fig. 8 Normalized parasitic center shift of the TRIVOT and CFP versus crossing ratio of the flexures**

**3.3 Motion of the Sliders of the Slider-Pivot Joints.** The motion of the sliders corresponds to the change in distance  $|B'D'|$  between the mobile extremities of the connecting rods (Fig. 5(b)):

$$\Delta_{sp}(\theta) = 2 \sin\left(\frac{\pi}{3}\right) (|OB'(\theta)| - |OB'(0)|) \quad (8)$$

which, using Eq. (6) and series expansion, yields

$$\Delta_{sp}(\theta) = \frac{-9\lambda^2 + 9\lambda - 1}{5\sqrt{3}\lambda} R\theta^2 + \mathcal{O}(\theta^4) \quad (9)$$

*Remark 1.* Based on Eqs. (5), (7), and (9), one can see that the pivots of the connecting rods perform a first-order motion ( $\propto \theta$ ) whereas the sliders perform a second-order motion ( $\propto \theta^2$ ). This

justifies the categorization between *main* and *secondary* flexures (Sec. 2.3) and the use of an accurate PRBM for the main flexures whereas the secondary are modeled using ideal sliders. ■

*Remark 2.* The PRBM developed by Pei et al. [38] enables to capture the parasitic motion of flexures, which is essential to accurately model the flexures that contribute predominantly to the motion of the TRIVOT, but was deemed negligible for the secondary flexures. Indeed, the parasitic motion of these flexures is of second order of their deflection [39, Eq. (5.13)] and hence becomes a fourth-order motion in the TRIVOT ( $\propto \theta^4$ ). A PRBM with greater accuracy can be obtained by modeling the secondary flexures with the same PRBM as the main flexures. The reason is that their boundary conditions are similar, assuming that the instantaneous center of rotation of each flexure is placed at infinity [38]. Such PRBM is depicted in Fig. 6. This however significantly increases the complexity of the model and is beyond the scope of this article. ■

## 4 Center Shift, Rotational Stiffness, and Maximum Stroke

This section analyzes critical properties of flexure pivots that differ from ideal pivots and need to be taken into account when dimensioning: the parasitic center shift, rotational stiffness, and angular stroke limit. Formulas are derived for the TRIVOT using the PRBM of Sec. 3, validated by FEM, and compared to our benchmark, the CFP, for different crossing ratios  $\lambda$ . In order to compare TRIVOT and CFP architectures with similar external diameter, we chose to keep the distance  $R$  from the center of the system to the mobile extremity of the flexures constant in all results (see Figs. 2(b) and 4(a)). Note that the results are based on a kinematic analysis of the TRIVOT and that the effect of external loads is not treated in this article.

**4.1 Finite Element Method Model.** The FEM results were performed using the commercial FEM software ANSYS [40]. The TRIVOT was meshed with hexahedral SOLID186 elements refined on the flexures such that there are three elements across their thickness, five along their height and a number of elements along the length conferring them a square face (Fig. 7). Although all analytical results of this section are dimensionless and hence applicable to architectures with different dimensions and materials, the following properties based on the mock-up of Fig. 3 were used for the FEM simulations:

- $R = 50$  mm
- Height of all the flexures (out of the rotation plane),  $b = 5$  mm
- Thickness of the main flexures (in the rotation plane),  $h = 1$  mm
- Thickness of the secondary flexures,  $h_2 = 0.5$  mm ( $h_2 = 1$  mm in the mock-up)
- Length of the parallel flexures,  $L_2 = 20$  mm
- Length of the slider-pivot flexures,  $L_3 = 35$  mm
- Young's modulus,  $E = 3$  GPa (polyoxymethylene (POM))
- Poisson's ratio,  $\nu = 0.44$  (POM)

**4.2 Parasitic Center Shift.** The main advantage of the TRIVOT in comparison to other CFPs is its reduced parasitic center shift. This is demonstrated by comparing its center shift to that of the CFP for a 15 deg rotation with different values of the crossing ratio  $\lambda$  (Fig. 8).

According to the PRBM in Fig. 5, the parasitic shift of the TRIVOT is zero (see kinematic explanation in Sec. 2.1). It is known that this is an approximation since the PRBM of the main flexures is already an approximation and mostly because the parasitic motion of the secondary flexures was neglected, assuming that fourth-order motions are negligible for small rotation. This approximation was verified by FEM (Fig. 8). A rotation was applied on the mobile body of the TRIVOT and the motion of a point on the mobile

body located at point  $O$  in the nominal position was computed. The norm of the parasitic center shift  $D = \sqrt{D_x^2 + D_y^2}$  is used for comparison, where  $D_x$  and  $D_y$  are the components of this motion along the  $xy$ -coordinates depicted in Fig. 5. To make the results independent of size, they are normalized by  $R$  using  $\tilde{D} = D/R$ .

For the CFP, the parasitic shift was computed using Ref. [19, Eq. (17.1)–(17.2)], assuming orthogonal flexures ( $\alpha = \pi/2$ ). Note that these formulas give the center shift components normalized by the flexure length  $L$ , namely  $dx = D_x/L$  and  $dy = D_y/L$ . For our comparison, we hence use

$$\tilde{D} = \frac{L\sqrt{dx^2 + dy^2}}{R} = \frac{\sqrt{dx^2 + dy^2}}{\lambda} = \frac{9\lambda^2 - 9\lambda + 1}{15\lambda \cos \alpha} \theta^2 + \mathcal{O}(\theta^3) \quad (10)$$

It is worth remembering that the PRBM of the TRIVOT could be improved using a sub-PRBM for each secondary flexures, see Remark 2. Nevertheless, our model already takes into account parasitic motions up to the second order ( $\propto \theta^2$ ), which is a good approximation in the case of the CFP [21,38], and shows that they are canceled. This result is validated by the comparison in Fig. 8 which shows that the FEM parasitic shift of the TRIVOT is reduced by one order of magnitude in comparison to the CFP for the entire range of parameter  $\lambda$  except a narrow region around  $\lambda = 87.3\%$  that is known to minimize the CFP center shift [17]. In this region, a more advanced model would be required for comparison.

*Remark 3.* Be aware that the effect of radial loads on the parasitic center shift is not taken into account here. This effect, which has been studied for the CFP [19], is not negligible and should be considered when relevant for a practical application. In the case of the TRIVOT, this effect not only depends on the main flexures but also on the dimensions and position of the secondary flexures. It is hence considered beyond the scope of this article, whose aim is to show that the geometry of the TRIVOT inherently reduces the parasitic shift, based on a simple kinematic analysis. Note that the radial stiffness of the TRIVOT is still evaluated in Sec. 5 for an example of application. ■

*Remark 4.* The PRBM of the TRIVOT assumes a symmetrical behavior for clockwise and counter clockwise rotations. The flexure implementation, however, has a rotational, but no axial symmetry (Fig. 2(b)). This asymmetry only concerns the secondary flexures and it is hence assumed that the consequences will only be apparent for large deformations or in the study of nonlinear effects. This is verified through FEM analysis by including results for both directions of rotation. The results show that the effect on the center shift is negligible and validate our assumption (Fig. 8). This verification will also be included in the subsequent results (Secs. 4.3 and 4.4). ■

*Remark 5.* The results are shown for  $0.5 \leq \lambda \leq 1.3$ , which is assumed to be the region of interest of this parameter for our design. For larger values ( $\lambda > 1.3$ ), the stroke becomes too limited for practical applications, see Sec. 4.4. For lower values ( $\lambda < 0.5$ ), the fixed body is further from the center of the system than the intermediate bodies, which complicates the design without bringing apparent advantages. In fact, due to the symmetry of the system, this corresponds essentially to inverting the boundary conditions on the main flexures and results in similar properties for  $\lambda$  and  $\lambda' = 1 - \lambda$  [19]. ■

**4.3 Rotational Stiffness.** The rotational stiffness of the TRIVOT can be estimated using the PRBM of Sec. 3. First, the strain energy of the system for a given rotation  $\theta$  of the mobile part is computed. This corresponds to the sum of the strain energies of each elastic joint of the PRBM

$$U = 3 \left( \int_0^{\theta_C} k_{t\mu} d\mu + \int_0^{\Delta_s} k_{s\mu} d\mu + \int_0^{\Delta_{sp}} k_{sp\mu} d\mu \right) \quad (11)$$

The rotational stiffness of the TRIVOT is then obtained by substituting Eqs. (5), (7), and (9) into Eq. (11) and deriving and

dividing  $U$  by  $\theta$ :

$$\begin{aligned} k_T = \frac{1}{\theta} \frac{dU}{d\theta} &= 3 \left( \frac{2}{15} \left( 9\lambda + \frac{1}{\lambda} - 9 \right) + 1 \right)^2 k_t \\ &+ \left( \frac{2(k_s + 3k_{sp})R^2(9\lambda^2 - 9\lambda + 1)^2}{75\lambda^2} \right. \\ &\left. + \frac{4(9\lambda^2 - 9\lambda + 1)(18\lambda^2 - 33\lambda + 2)(18\lambda^2 - 3\lambda + 2)^2 k_t}{50625\lambda^4} \right) \theta^2 \\ &+ \mathcal{O}(\theta^4) \end{aligned} \quad (12)$$

This shows that the stiffness of the TRIVOT consists of a constant term that only depends on the main flexures and higher order terms that are function of the rotation angle, where the secondary flexures also contribute. Assuming that the TRIVOT performs small rotations, neglecting the higher order terms provides a good approximation and substituting the spring constant of the main flexures with the value from the PRBM [38, Eq. (15)]

$$k_t = \frac{900EI\lambda^3(3\lambda^2 - 3\lambda + 1)}{(18\lambda^2 - 3\lambda + 2)^2 R} \quad (13)$$

yields

$$k_T = \frac{12EI}{L} (3\lambda^2 - 3\lambda + 1) + \mathcal{O}(\theta^2) \quad (14)$$

where  $I$  is the area moment of inertia of the main flexures' cross section. It is worth noticing that this corresponds to 1.5 times the rotational stiffness of the CFP [20, Eq. (12)]. This was expected since the main flexures have the same boundary conditions in both architectures, with the difference that there are three of them in the TRIVOT as opposed to two in the CFP.

In order to provide results that are independent from size and material, the rotational stiffness of the TRIVOT was normalized as follows:

$$\tilde{k}_T = \frac{R}{EI} k_T = 12\lambda(3\lambda^2 - 3\lambda + 1) \quad (15)$$

In order to validate Eq. (15) and to show the influence of the flexures' crossing ratio on the stiffness of the TRIVOT, analytical and FEM results for  $\tilde{k}_T$  versus  $\lambda$  are plotted in Fig. 9. The FEM stiffness was obtained by computing the reaction torque on the fixed frame for a 1 deg rotation of the mobile body. The analytical results match the FEM results with less than 3% discrepancy, thus

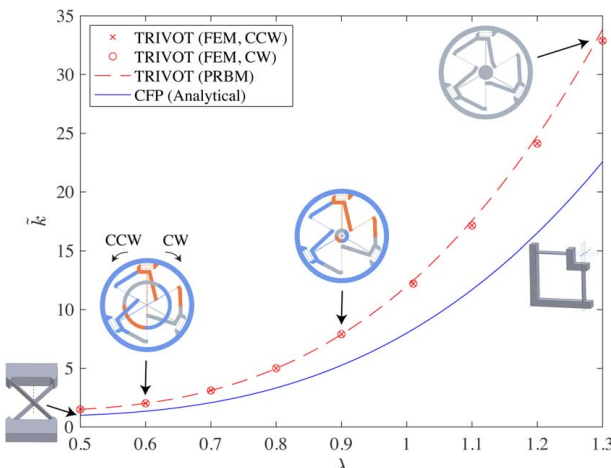


Fig. 9 Normalized rotational stiffness of the TRIVOT and CFP versus crossing ratio of the flexures

providing validation for our formula. For larger rotations, Eq. (12) can be used, where the spring constants of the secondary flexures are given in Sec. 3. For comparison, Fig. 9 also displays the normalized stiffness of the CFP, namely, 2/3 of the TRIVOT stiffness.

**4.4 Admissible Angular Stroke.** The maximum range of motion of a compliant mechanism is determined by the stress in its flexures. The PRBM of Sec. 3 shows that the main flexures are subjected to the largest deformation and, since all flexures have similar dimensions, it is assumed the maximum stress will be reached there. For a given admissible stress  $\sigma_{adm}$  in the material, the maximum angular stroke of the TRIVOT can hence be computed using the PRBM of the main flexures [38, Eq. (18)]:

$$\theta_{max} = \frac{\sigma_{adm} L}{Eh(3\lambda - 1)} \quad (16)$$

Note that the same formula applies to the maximum angular stroke of the CFP [20, Eqs. (23)–(27)] which was again expected since the CFP flexures are subjected to the same boundary conditions as the TRIVOT main flexures.

In order to validate this formula and to show the influence of the flexures' crossing ratio on the admissible stroke of the TRIVOT, Fig. 10 shows FEM and analytical values of  $\theta_{max}$  versus  $\lambda$  for the chosen implementation. The FEM results are based on the von Mises stress in the main flexures for an applied rotation on the mobile body. We chose an admissible elastic strain  $\epsilon_{adm} = \sigma_{adm}/E = 0.4\%$ , which can typically be reached with steel alloys, titanium alloys, polymers, glass, or silicon [39, Table B.14], [41,42]. The thickness  $h$  of the main flexures is constant for all designs and satisfies  $\tilde{h} = h/R = 0.02$ . We chose this value to have flexure aspect ratios that are compatible with standard micromachining techniques such as wire electro-discharge machining (EDM).

In order to make the result independent of size and material, Eq. (16) can now be rewritten in terms of the dimensionless parameters introduced above:

$$\theta_{max} = \frac{\epsilon_{adm}}{\tilde{h}\lambda(3\lambda - 1)} \quad (17)$$

The analytical results match the FEM results with less than 5% discrepancy for  $\lambda \geq 0.65$ , thus providing validation for our formula. For  $\lambda \leq 0.65$ , the admissible rotation angles become large ( $\theta_{max} > 20$  deg) and the parasitic rotation caused by the asymmetry of our implementation with respect to the plane of rotation is

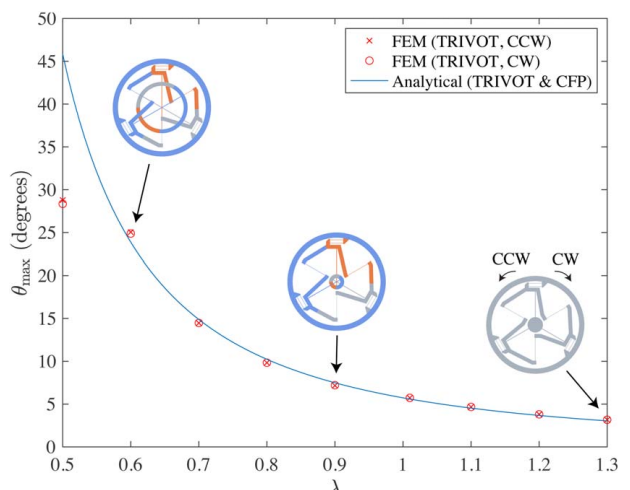
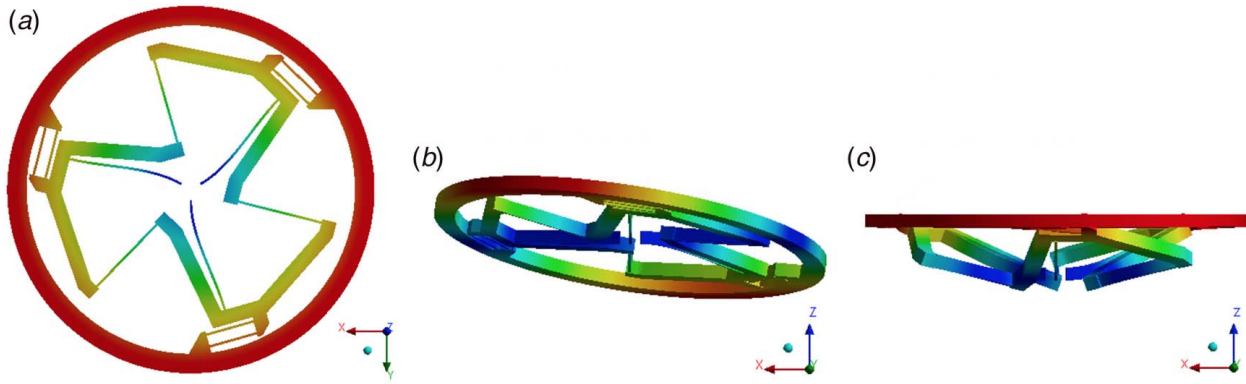


Fig. 10 Admissible angular stroke of a TRIVOT and CFP with  $\epsilon_{adm} = 0.4\%$  and  $\tilde{h} = 0.02$  versus the crossing ratio of the flexures



**Fig. 11** First four mode shapes (a)  $f_1 = 8.05$  Hz (rotational DOF), (b)  $f_2 = f_3 = 35.5$  Hz (out-of-plane tilting DOC), and (c)  $f_4 = 43.1$  Hz (out-of-plane translational DOC) of the design in Fig. 3 with dimensions given in Sec. 4.1 obtained by finite element modal analysis. The tone scale represents arbitrary motion amplitudes with respect to the rest position.

**Table 1** Support stiffness of the lowest unwanted modes of the TRIVOT design in Fig. 11

	Mode 1	Modes 2 and 3	Mode 4
Eigenfrequency, $f$	8.05 Hz	35.5 Hz	43.1 Hz
Inertia	$J_z = 1.71 \cdot 10^{-4}$ kg/m <sup>3</sup>	$J_x = J_y = 8.58 \cdot 10^{-5}$ kg/m <sup>3</sup>	$m = 4.39 \cdot 10^{-2}$ kg
Stiffness, $k$	0.44 N m/rad	4.27 N m/rad	$3.22 \cdot 10^3$ N/m

Note: The stiffness values are approximations based on the assumption that all the parts of the system perform the same motion ( $k = 4\pi^2f^2J$  for rotations and  $k = 4\pi^2f^2m$  for translations).

no longer negligible (three different superimposed levels in Fig. 4(b)). This parasitic rotation about an axis perpendicular to the main rotation axis subjects the flexures to additional torsion and bending stresses. For crossing ratios around  $\lambda = 0.5$ , Fig. 10 shows that this significantly reduces the admissible angular stroke. This issue can however be solved by using a symmetrically stacked architecture by, for instance, using five levels (similarly to the CFP with three [17, Fig. 1] or four [15, Fig. 1] flexures or by using interlocked lattice flexures [43]. If this is the case, it is assumed that the admissible stroke would be close to the predictions of Eq. (17).

*Remark 6.* Bear in mind that the admissible stroke of the TRIVOT depends on the material and dimensions. For instance, the architectures with  $\lambda > 1$  in Fig. 10 have a flexure aspect ratio  $L/h < 50$  that could be increased without compromising manufacturability in order to reach greater angular stroke. The mock-up in Fig. 3 also achieves a larger rotation angle due to the high admissible strain of its material ( $\epsilon_{\text{adm}} \approx 2.3\%$ ). ■

## 5 Preliminary Support Stiffness Analysis Based on an Oscillator Design

For the TRIVOT mechanism to effectively act as a pivot joint, a high radial and out-of-plane stiffness is required. In other words, the stiffness of the mechanism along its degrees-of-constraint (DOC) must be significantly higher than about its rotational DOF. As these properties depend on the dimensions of the TRIVOT, we propose a preliminary study based on a mechanical watch time base application. This is motivated by the fact that flexure oscillators are promising time bases thanks to their high quality factor and monolithic design compatible with microfabrication [13,14,27,28,30]. This case study is based on the mock-up design in Fig. 3, whose dimensions are given in Sec. 4.1 and whose proportions are scalable to watch scale ( $\approx 10$  times smaller diameter). The center part is fixed and the inertia is concentrated on the mobile body, reflecting the characteristics of a balance wheel.

For an oscillator application, a common way of ensuring sufficient support stiffness is to make sure that the eigenfrequencies of the unwanted oscillation modes are far enough from the eigenfrequency of the main (useful) mode ( $\approx 10$  times higher). A modal analysis of the system is hence performed with the model described in Sec. 4.1 and a material density  $\rho = 1410$  kg/m<sup>3</sup> corresponding to POM (Fig. 11). This method, which has the advantages of being computationally inexpensive and allowing to compare rotational and translational stiffness components, has also been used previously to optimize the support stiffness of flexure mechanisms [44,45]. For applications where the actual stiffness values are required, they can be derived from the eigenfrequencies using the inertia of the system, see Table 1.

The results show that the structure effectively fulfills the pivot function since the first mode is a rotation about the desired axis whose eigenfrequency is clearly differentiated from the lowest unwanted mode ( $f_2 = 4.4f_1$ ). The out-of-plane support stiffness, despite being almost 10 times larger than the rotational stiffness, could be increased in order to provide sturdier pivot guidance. This can be achieved by increasing the dimension  $b$  of the TRIVOT along its rotation axis.

The modal analysis was thus repeated on a design with flexures whose height  $b'$  is 20 times larger than their thickness (as opposed to 5 times previously). This cross-sectional aspect ratio is compatible with standard micromanufacturing techniques such as EDM. With this modification, the out-of-plane modes were moved further away from the first eigenfrequency: the lowest unwanted frequency became the in-plane translation ( $f_2 = f_3 = 9.2f_1$ ). The in-plane support stiffness was then further improved by increasing the thickness of the secondary flexures to  $h_2 = 1.5h$ . The resulting modal analysis is shown in Fig. 12. With this design, the lowest unwanted eigenfrequency is 13.5 times higher than the first eigenfrequency, which is considered sufficient for the desired application. In terms of stiffness, the out-of-plane support stiffness is now two orders of magnitude greater than the rotational stiffness (Table 2).

Note that the parameters used to improve the support stiffness (the out-of-plane height of the flexures and thickness of the secondary

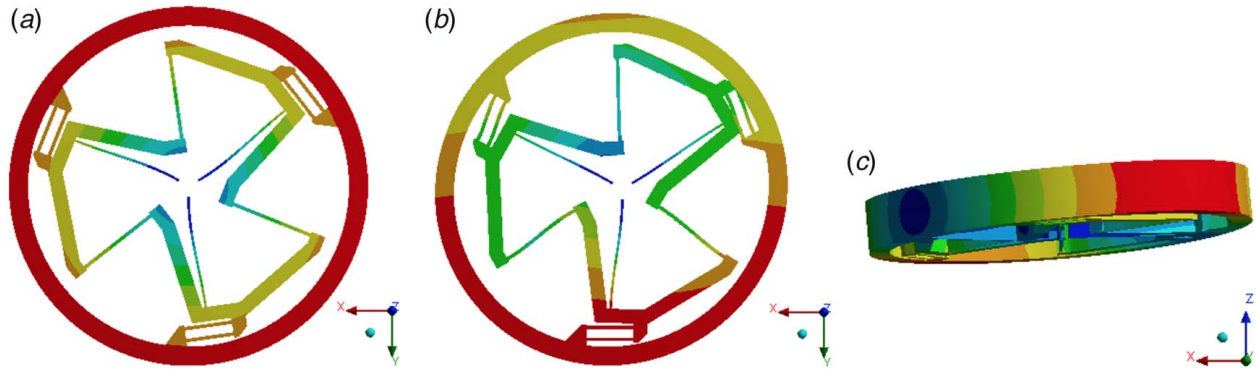


**Fig. 12** First five mode shapes (a)  $f_1 = 8.37$  Hz (rotational DOF), (b)  $f_2 = f_3 = 113$  Hz (in-plane translational DOF), and (c)  $f_4 = f_5 = 119$  Hz (out-of-plane tilting DOF) of the design in Fig. 3 with the same dimension as in Fig. 11 but an increased height  $b' = 20$  mm and an increased secondary flexure thickness  $h_2 = 1.5h = 1.5$  mm. The results are obtained by finite element modal analysis. The tone scale represents arbitrary motion amplitudes with respect to the rest position.

**Table 2 Support stiffness of the lowest unwanted modes of the TRIVOT design in Fig. 12**

	Mode 1	Modes 2 and 3	Modes 4 and 5
Eigenfrequency, $f$	8.37 Hz	113 Hz	119 Hz
Inertia	$J_z = 6.93 \cdot 10^{-4}$ kg/m <sup>3</sup>	$m = 0.179$ kg	$J_x = J_y = 3.53 \cdot 10^{-4}$ kg/m <sup>3</sup>
Stiffness, $k$	$1.92 \cdot 10^4$ N/mrad	$9.02 \cdot 10^4$ N/m	$197$ N m/rad

Note: The stiffness values are approximations based on the assumption that all the parts of the system perform the same motion ( $k = 4\pi^2f^2J$  for rotations and  $k = 4\pi^2f^2m$  for translations).

**Table 3 Qualitative comparison between TRIVOT and CFP properties**

Flexure pivot	Reduced parasitic shift	Maximized angular stroke	Planar design	RCC
TRIVOT with $\lambda = 0.5$	Yes	Yes	No	No
TRIVOT with $\lambda > 1$	Yes	No	Yes	Yes
CFP with $\lambda = 0.5$	No	Yes	No	No
CFP with $\lambda = 0.873$	Yes	No	No	No
CFP with $\lambda > 1$	No	No	Yes	Yes

flexures) have a minor impact on the performance criteria previously discussed in this article. Indeed, the parasitic shift and maximum angular stroke of the pivot are function of its in-plane dimensions and are predominantly defined by the main flexures, see Secs. 4.2 and 4.4. The nominal rotational stiffness of the TRIVOT is also defined only by its main flexures and is hence not impacted by  $h_2$ , see Eq. (14). It is, however, impacted by the height of the flexures in a proportional manner. In summary, we provided effective tools to increase the support stiffness of the TRIVOT for a given application, manufacturing technique and available volume.

## 6 Conclusion

In this article, we presented the design of a novel flexure pivot whose ideal kinematics achieve a pure rotation without overconstraint. We showed different configurations, characterized by the crossing ratio of the main flexures, allowing to either maximize the admissible angular stroke for given flexures or to have a planar design. We demonstrated that these properties could be achieved while maintaining a very small parasitic center shift, which is not the case with our CFP benchmark (see comparison in Table 3). These improvements nevertheless increase complexity, with six times more flexures than the CFP and a fabrication over at least three levels in the configuration with crossing flexures. Overall, the TRIVOT design is an improvement over other flexure pivots that achieve similar properties but have the drawback

of having either overconstraints, internal degrees-of-freedom, or elasticity in one of the bodies.

By solving the issue of parasitic center shift, which is a common obstacle to the replacement of traditional bearings with flexure pivots, the TRIVOT paves the way to new applications that could benefit from its absence of play, contact friction, wear, polluting debris, need for lubrication, and its possible monolithic fabrication. Additionally, the TRIVOT provides a new way of implementing a remote (i.e., virtual) center of rotation, which is not possible with traditional bearings and advantageous in numerous applications. Our future research directions include the experimental validation of the results presented here, the study of the stiffness nonlinearity of the TRIVOT, and a dimensioning for a mechanical watch oscillator application.

## Acknowledgment

We thank Ilan Vardi for his constructive criticism and careful review of the manuscript. We also thank Arnaud Maurel for his assistance in fabricating the mock-up in Fig. 3.

## Conflict of Interest

There are no conflicts of interest.

## Data Availability Statement

The datasets generated and supporting the findings of this article are obtainable from the corresponding author upon reasonable request.

## References

- [1] Helmer, P., 2006, "Conception Systématique de Structures Cinétiques Orthogonales Pour La Microrobotique," Ph.D. thesis, EPFL, Lausanne.
- [2] Richard, M., and Clavel, R., 2010, "A New Concept of Modular Kinematics to Design Ultra-High Precision Flexure-Based Robots," *ISR* 2010 (41st International Symposium on Robotics) and ROBOTIK 2010 (6th German Conference on Robotics), Munich, Germany, June 7–9, pp. 1–8.
- [3] Jayanth, G. R., and Menq, C. H., 2014, "Design and Modeling of an Active Five-Axis Compliant Micromanipulator," *ASME J. Mech. Rob.*, **6**(4), p. 041014.
- [4] Yu, J., Xie, Y., Li, Z., and Hao, G., 2015, "Design and Experimental Testing of an Improved Large-Range Decoupled XY Compliant Parallel Micromanipulator I," *ASME J. Mech. Rob.*, **7**(4), p. 044503.
- [5] Verotti, M., Dochshanov, A., and Belfiore, N. P., 2017, "A Comprehensive Survey on Microgrippers Design: Mechanical Structure," *ASME J. Mech. Des.*, **139**(6), p. 060801.
- [6] Seelig, F. A., 1968, "Flexural Pivots for Space Applications," Proceedings of the 3rd Aerospace Mechanisms Symposium, California Institute of Technology, May 23–24, pp. 9–18.
- [7] Henein, S., Spanoudakis, P., Droz, S., Myklebust, L. I., and Onillon, E., 2003, "Flexure Pivot for Aerospace Mechanisms," Proceedings of the 10th ESMATS, San Sebastian, Spain, Sept. 25, pp. 1–4.
- [8] Huo, T., Yu, J., and Zhao, H., 2020, "Design of a Kinematic Flexure Mount for Precision Instruments Based on Stiffness Characteristics of Flexural Pivot," *Mech. Mach. Theory*, **150**, p. 103868.
- [9] Zanaty, M., Fussinger, T., Rogg, A., Lovera, A., Lambelet, D., Vardi, I., Wolfensberger, T. J., Baur, C., and Henein, S., 2019, "Programmable Multistable Mechanisms for Safe Surgical Puncturing," *J. Med. Dev.*, **13**(2), p. 021002.
- [10] Fifanski, S. K., 2020, "Flexure-Based Mecano-Optical Multi-Degree-of-Freedom Transducers Dedicated to Medical Force Sensing Instruments," <https://infoscience.epfl.ch/record/278197>
- [11] Thomas, T. L., Kalpathy Venkiteswaran, V., Ananthasuresh, G. K., and Misra, S., 2021, "Surgical Applications of Compliant Mechanisms: A Review," *ASME J. Mech. Rob.*, **13**(2), p. 020801.
- [12] Robuschi, N., Braghini, F., Corigliano, A., Ghisi, A., and Tasora, A., 2017, "On the Dynamics of a High Frequency Oscillator for Mechanical Watches," *Mech. Mach. Theory*, **117**, pp. 276–293.
- [13] Thalmann, E., 2020, "Flexure Pivot Oscillators for Mechanical Watches," Ph.D. thesis, EPFL, Lausanne.
- [14] Schneegans, H., Thalmann, E., and Henein, S., 2021, "Shaking Force Balancing of a 2-DOF Isotropic Horological Oscillator," *Precis. Eng.*, **72**, pp. 502–520.
- [15] Wittrick, W., 1948, "The Theory of Symmetrical Crossed Flexure Pivots," *Aust. J. Sci. Res. A Phys. Sci.*, **1**, p. 121.
- [16] Haringx, J. A., 1949, "The Cross-Spring Pivot as a Constructional Element," *Flow Turbulence Combust.*, **1**(1), p. 313.
- [17] Wittrick, W., 1951, "The Properties of Crossed Flexure Pivots, and the Influence of the Point at Which the Strips Cross," *Aeronaut. Q.*, **2**, pp. 272–292.
- [18] Pei, X., Yu, J., Zong, G., Bi, S., and Yu, Z., 2008, "Analysis of Rotational Precision for an Isosceles-Trapezoidal Flexural Pivot," *ASME J. Mech. Des.*, **130**(5), p. 052302.
- [19] Zhao, H., and Bi, S., 2010, "Accuracy Characteristics of the Generalized Cross-Spring Pivot," *Mech. Mach. Theory*, **45**(10), pp. 1434–1448.
- [20] Zhao, H., and Bi, S., 2010, "Stiffness and Stress Characteristics of the Generalized Cross-Spring Pivot," *Mech. Mach. Theory*, **45**(3), pp. 378–391.
- [21] Marković, K., and Zelenika, S., 2015, "Characterization of Cross-Spring Pivots for Micropositioning Applications," Barcelona, Spain, May 21, SPIE Microtechnologies, p. 951727.
- [22] Xu, Q., 2013, "Design and Implementation of a Novel Rotary Micropositioning System Driven by Linear Voice Coil Motor," *Rev. Sci. Instrum.*, **84**(5), p. 055001.
- [23] Henein, S., 2012, "Short Communication: Flexure Delicacies," *Mech. Sci.*, **3**(1), pp. 1–4.
- [24] Cosandier, F., Henein, S., Richard, M., and Rubbert, L., 2017, *The Art of Flexure Mechanism Design*, EPFL Press, Lausanne.
- [25] Kahrobaian, M. H., Thalmann, E., Rubbert, L., Vardi, I., and Henein, S., 2018, "Gravity-Insensitive Flexure Pivot Oscillators," *ASME J. Mech. Des.*, **140**(7), p. 075002.
- [26] Kahrobaian, M. H., Thalmann, E., and Henein, S., 2020, "Flexure Pivot Oscillator Insensitive to Gravity," Jan, Patent Number WO2020016131.
- [27] Thalmann, E., Kahrobaian, M. H., Vardi, I., and Henein, S., 2020, "Flexure Pivot Oscillator With Intrinsically Tuned Isochronism," *ASME J. Mech. Des.*, **142**(7), p. 075001.
- [28] Thalmann, E., and Henein, S., 2021, "Optical Measurement Method for Mechanical Time Base Characterization," Proceedings of the 21st International Conference of the European Society for Precision Engineering and Nanotechnology, EUSPEN 2021, Virtual, Online, June 7–10, pp. 469–472.
- [29] Liu, L., Bi, S., Yang, Q., and Wang, Y., 2014, "Design and Experiment of Generalized Triple-Cross-Spring Flexure Pivots Applied to the Ultra-Precision Instruments," *Rev. Sci. Instrum.*, **85**(10), p. 105102.
- [30] Thalmann, E., and Henein, S., 2021, "Design of a Flexure Rotational Time Base With Varying Inertia," *ASME J. Mech. Des.*, **143**(11), p. 115001.
- [31] Ciblak, N., and Lipkin, H., 2003, "Design and Analysis of Remote Center of Compliance Structures," *J. Robot. Syst.*, **20**(8), pp. 415–427.
- [32] Lai, L.-J., and Zhu, Z.-N., 2016, "Modeling and Analysis of a Compliance Model and Rotational Precision for a Class of Remote Center Compliance Mechanisms," *Appl. Sci.*, **6**(12), p. 388.
- [33] Pei, X., Yu, J., Zong, G., Bi, S., and Hu, Y., 2009, "A Novel Family of Leaf-Type Compliant Joints: Combination of Two Isosceles-Trapezoidal Flexural Pivots," *ASME J. Mech. Rob.*, **1**(2), p. 021005.
- [34] Thalmann, E., and Henein, S., 2021, "Design of a Triple Crossed Flexure Pivot With Minimized Parasitic Shift," *Proceedings of the ASME 2021 IDETC-CIE Conference*, ASME, Virtual, Online, Aug. 17–19, p. V08AT08A003.
- [35] Grübler, M., 1917, *Getriebelehre: Eine Theorie Des Zwanglaufes Und Der Ebenen Mechanismen*, Springer-Verlag, Berlin.
- [36] Howell, L. L., Magleby, S. P., and Olsen, B. M., 2013, *Handbook of Compliant Mechanisms*, Wiley, Hoboken, NJ.
- [37] Howell, L. L., 2001, *Compliant Mechanisms*, Wiley, New York.
- [38] Pei, X., Yu, J., Zong, G., and Bi, S., 2010, "An Effective Pseudo-Rigid-Body Method for Beam-Based Compliant Mechanisms," *Precis. Eng.*, **34**(3), pp. 634–639.
- [39] Henein, S., 2000, "Conception Des Structures Articulées à Guidages Flexibles De Haute Précision," Ph.D. thesis, EPFL, Lausanne.
- [40] ANSYS, 2018, ANSYS® Workbench, Release 19.2, ANSYS Workbench User's Guide, ANSYS, Inc., Canonsburg, PA.
- [41] Henein, S., Barrot, F., Jeanneret, S., Fournier, R., Giriens, L., Gumy, M., Droz, S., and Toimil, M., 2011, "Silicon Flexures for the Sugar-Cube Delta Robot," Proceedings of the 11th Euspen International Conference, Como, Italy, May 23–26, p. 4.
- [42] Bellourard, Y., 2011, "On the Bending Strength of Fused Silica Flexures Fabricated by Ultrafast Lasers," *Opt. Mater. Exp.*, **1**(5), pp. 816–831.
- [43] Kiener, L., Saudan, H., Cosandier, F., Perruchoud, G., and Spanoudakis, P., 2019, "Innovative Concept of Compliant Mechanisms Made by Additive Manufacturing," *9th EASN International Conference on Innovation in Aviation & Space*, Athens, Greece, Sept. 3–6, p. 07002.
- [44] Wiersma, D. H., Boer, S. E., Aarts, R., and Brouwer, D. M., 2012, "Large Stroke Performance Optimization of Spatial Flexure Hinges," International Design Engineering Technical Conferences and Computers and Information in Engineering Conference, Vol. 45059, Chicago, IL, Aug. 12–15, American Society of Mechanical Engineers, pp. 115–124.
- [45] Gunnink, K., Aarts, R., and Brouwer, D. M., 2013, "Performance Optimization of Large Stroke Flexure Hinges for High Stiffness and Eigenfrequency," Proceedings of the 28th Annual Meeting of the American Society for Precision Engineering (ASPE), Saint Paul, MN, Oct. 20–25, ASPE, pp. 1–6.